Effect of field-line chaos on Plasma Filament Dynamics and Turbulence in the Scrape-Off Layer

D. Meyerson[‡], C. Michoski[⋆], F. Waelbroeck[‡], W. Horton[‡]

Institute for Fusion Studies (IFS)[‡], Department of Physics[‡]

Institute for Computational Engineering and Sciences (ICES)[⋆],

Department of Aerospace Engineering and Engineering Mechanics[⋆]

University of Texas at Austin, Austin, TX 78712

March 28, 2014

Abstract

Naturally occurring error fields as well as resonant magnetic perturbations applied for stability control are known to cause magnetic field-line chaos in the scrape-off layer (SOL) region of tokamaks. Here, 2D simulations are used to investigate the effect of the field-line chaos on the SOL and in particular on its width and peak particle flux. The chaos enters the SOL dynamics through the connection length, which is evaluated using a Poincaré map. The variation of experimentally relevant quantities, such as the SOL gradient length scale and the intermittency of the particle flux in the SOL, is described as a function of the strength of the magnetic perturbation. It is found that the effect of the chaos is limited to the broadening of the profile of the sheath-loss coefficient, which is proportional to the inverse connection length. That is, the SOL transport in a chaotic field is equivalent to that in a model where the sheath-loss coefficient is replaced by its average over the unperturbed flux surfaces.

Contents

1 Introduction

In diverted tokamaks, the separatrix defines the boundary between open and closed flux surfaces and acts as a riverbed for the scrape-off layer (SOL). In the SOL, the flow across the magnetic field balances the parallel streaming along the field towards the plasma-facing components (PFC). A picture of how tokamak turbulence and transport in the SOL scale with experimentally controllable parameters is necessary to minimize peak heat and particle flux loads on the PFC,[25] to minimize introduction of impurities, and simultaneously maintain conditions that are consistent with global plasma confinement.[18, 29, 26, 12] In the presence of edge-resonant non-axisymmetric perturbations, however, the separatrix is readily shattered and replaced by a region exhibiting field-line chaos, or magnetic stochasticity. The effect of stochasticity effect is manifested by the splitting of the separatrix footprints [46]. Field-line chaos can be introduced by deliberately applied resonant Magnetic Perturbations (RMPs) [24], ergodic magnetic limiters [31, 22] and naturally-occurring instabilities. RMPs have been the subject of intense recent interest for their use in controlling edge localized modes by keeping the edge pedestal conditions below some critical threshold and by effectively replacing impulsive intermittent ELM transport with a series of smaller less disruptive transport events, or even with full suppression [17].

While the SOL has a complex three dimensional geometry, its physics is dominated by curvature-driven interchange instabilities characterized by a short extension across but a long extension along the field lines.[12] Following standard practice, we average vorticity and density equations along the field-aligned dimension and work in the resulting 2D plane normal to the field-lines. Excluding regimes where full drift-wave physics has a strong influence on the dynamics [2, 1], this dimensionally-reduced approach has provided experimentally validated descriptions of turbulent transport, interplay between zonal flows and turbulence,[36, 43, 47] creation of coherent structures, and SOL density length scales, among other results [44, 27, 50, 11, 20, 36]. End-losses along the field appear as a damping term in the density equation with a coefficient inversely proportional to the connection length $L_\parallel$. In this paper we specify $L_\parallel$ by a map that describes chaotic connection lengths in the region spanning the outer portions of the core and the SOL. To maintain the density in the presence of the end-losses, we include a particle source at the edge of the simulation domain that faces the core of the plasma. The resulting turbulence is thus flux-driven. The particle source can be thought of as modeling the injection of particles by neutral beams, pellets and recycling.

It is generally accepted that cross field transport in the region between the plasma edge and the vessel wall is dominated by intermittent transport [5, 44, 21] mediated by coherent, radially propagating plasma filaments called blobs.[27, 8, 19, 49] Typically the magnetic-curvature drift combined with the usual $\mathbf{E} \times \mathbf{B}$ convection will drive a blob radially outward. Continuity and charge conservation equations govern their dynamics. Blobs provide a mechanism for radial transport of heat and momentum that greatly exceeds neoclassical predictions.

The usefulness of blobs, as a concept, depends on their ability to survive long enough to affect transport and demonstrate a clear dependence of their properties on model plasma parameters. Blob lifetimes have been examined theoretically by Krasheninnikov [27] and other authors [35, 21] and experimentally in [8, 4]. These studies have shown the existence of a most stable blob size. The mechanisms underlying the interplay between parallel transport, diffusion, convective processes, and spontaneous formation of blobs affects the width of the SOL layer and the intermittency of transport. These mechanisms have been studied in some detail [12, 20, 3, 2, 43]. In this paper we examine how magnetic chaos, modeled with a chaotic map that mimics the application of static RMPs, changes statistical characterization of blobs and the scaling of blob properties with plasma parameters. As an example of how our current understanding of blob behavior may be challenged by the presence of chaos, consider the simplest analytic prediction of radial blob velocity - $V_x \propto L_\parallel/(R\delta_y^2)$. With the addition of a chaotic field, there will be large variations in the $L_\parallel$ value over the spatial footprint of the blob - possibly affecting its coherence and thus the mean particle transport and

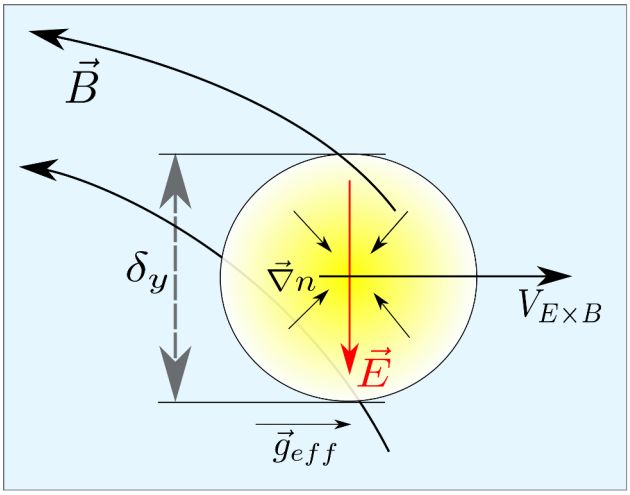

Figure 1: A simple blob with key forces, length scales and directions

intermittency of density fluctuations. From previous work we also know that for a constant α there is a strong selection for a specific blob size [3, 27]. It is natural to ask whether magnetic chaos might seed blobs of different sizes, or favor hole creation over blob creation. Such effects on blob dynamics would clearly affect the observed density scaling distance in SOL density profile. The aim of the present paper is to answer these questions within the framework of the 2D model of SOL transport.

The remainder of this paper is organized as follows. In Sec. 2, we describe the formulation of the problem and some simple analytic considerations. In Sec. 3, we address the scaling of the density length-scale and the selection of the dominant blob size. Sec. 3.5 examines the statistics of the turbulence and in particular the intermittency of particle transport. We conclude by summarizing and discussing our results in Sec. 4 .

2 Formulation and Analytic considerations

2.1 Formulation

We use a simple two fluid interchange model that nonetheless contains all the important features required; curvature and density gradient drifts, $E \times B$ driven turbulence, blob formation, and a parallel closure scheme that is able to model both closed and open field lines. Similar models have a been used by many authors and groups to study SOL turbulence, zonal flows and transport in both mirror machines and tokamaks edge plasmas [2, 51, 12, 3].

The equations used here have been normalized by the Bohm gyro-radius $\rho_s = c_s/\Omega_i$, ion gyro-frequency Ω_i, and ion-acoustic speed $c_s = \sqrt{kT_e/m_i}$. Terms containing coefficient α come from averaging parallel current and velocities given by elementary sheath theory. Notice that we assume no scale separation between some background and a perturbed portion. This is consistent with the observed character of the SOL layer. External density and momentum sources can be specified with S_n and S_ω respectively. In this work we set

$S_\varpi = 0$. We will discuss the choice of S_n in section 2.4.

$$\partial_t n + V_E \cdot \nabla n - D_n \nabla^2 n \ + \alpha n = S_n, \tag{1a}$$

$$\partial_t \varpi + V_E \cdot \nabla \varpi - D_\varpi \nabla^2 \varpi - \alpha \phi - \beta \frac{(b \cdot \nabla x \times \nabla n)}{n} = S_\varpi, \tag{1b}$$

$$\varpi = \nabla^2 \phi, \tag{1c}$$

$$V_E = b \times \nabla \phi, \tag{1d}$$

$$\beta = \frac{2\rho_s}{R_0} \text{ and } \alpha = \frac{2\rho_s}{L_\parallel} \tag{1e}$$

.

We are interested in how the presence of RMPs will influence transport in the region spanning the plasma edge and the vessel wall that is often dominated by coherent, radially propagating blobs or streamers. In arriving at equation (1) the full three dimensional geometry is reduced to two dimensions by averaging along the field lines, where we take the flute approximation [41] and assume that all introduced quantities vary weakly along uniform magnetic field lines. The influence of RMPs is thus reflected in the parallel connection length to the divertor that enters into the α parameter of equation (1).

2.2 Geometry

While BOUT++ is designed primarily for field aligned, non-orthogonal coordinates, it also allows for simulations in slab geometry. A shortcoming of the 2D slab model is that it is unable to account for the variation of the curvature along the field lines or for the resulting variation in the mode structure. Various estimates of the parallel wavenumber can be made. [51] Resolving the parallel mode structure requires a full three dimensional simulation. [40] Recent work [2] indicates substantial qualitative changes in the behavior of this system when the full three dimensional picture is taken into account. The simplifying nature of the 2D model, by contrast, enables a greater focus on properties that are independent of the 3D geometry of the SOL.

2.3 RMPs and the Ullmann Map

Magnetic fields have a field line structure governed by Hamilton's equations, with the toroidal angle playing the role of time. The field lines of axisymmetric equilibria lie on nested toroidal surfaces, constituting integrable Hamiltonian systems, and perturbations of such axisymmetric equilibria are naturally described by Poincaré sections, the intersection of field lines with a poloidal section. The Ullmann map [39] is a Poincaré magnetic field line map that was created to study the effects of an ergodic divertor on toroidal plasmas. Repeated application allows us to assign a parallel connection length value based on the number of applications necessary for a given field line to hit the divertor. One advantage of this map over some others is that it is characterized in terms of experimental quantities such as major and minor radius, I_{ext}/I_p and some safety factor, $q(r)$.

The connection lengths are said to exhibit chaos when two neighboring points are traversed by field lines that follow very different trajectories. For example, one field line may quickly terminate on the divertor or the wall while another may stay trapped. A parallel current closure may be assigned based on this computed chaotic parallel connection length.

The Ullmann map is a composition of a map with good flux surfaces, where

$$r_{n+1} = \frac{r_n}{1 - a_1 sin\theta_n}, \tag{2a}$$

$$\theta_{n+1} = \theta_n + \frac{2\pi}{q_{eq}(r_{n+1})} + a_1 cos\theta_n, \tag{2b}$$

and a perturbation map, given by

$$r_n = r_{n+1} + \frac{mC\epsilon b}{m-1}\left(\frac{r_{n+1}}{b}\right)^{m-1} sin\left(m\theta_n\right), \tag{3a}$$

$$\theta_{n+1} = \theta_n - C\epsilon\left(\frac{r_{n+1}}{b}\right)^{m-2} cos\left(m\theta_n\right). \tag{3b}$$

where q is the safety factor, C is a geometric factor, and ϵ is current in the external coil normalized by the plasma current

$$C = \frac{2mla^2}{R_0 b^2 q_a}, \tag{4a}$$

$$\epsilon = \frac{I_l}{I_p}, \tag{4b}$$

with $m = 2, 3, ...$

Given some effective minor radius a we can approximate the field-line length once we know how many applications of the map connect a given point to the divertor:

$$L_{\parallel} \approx q(a) 2\pi a N_{turns}. \tag{5}$$

Ultimately what enters equation (1) is the inverse of this parallel connection length, $\alpha = 2\rho_s / L_{\parallel}$.

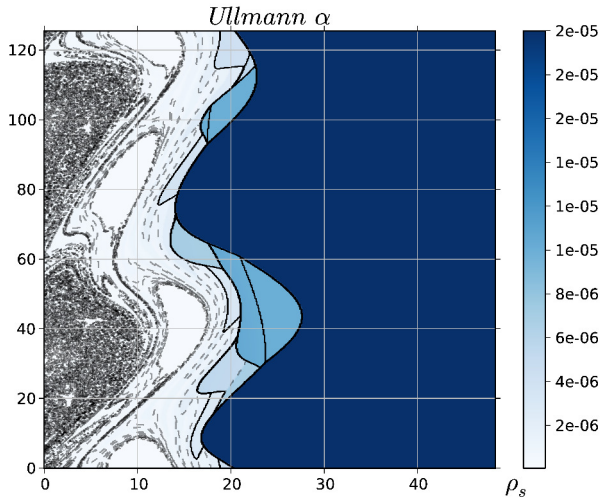

(a) Contour plot of the inverse connection length, α, associated with magnetic chaos generated by the Ullmann map. Escape basins appear as darker regions, whereas trapped regions appear white and have $\alpha = 0$. Note that the contour values change discretely.

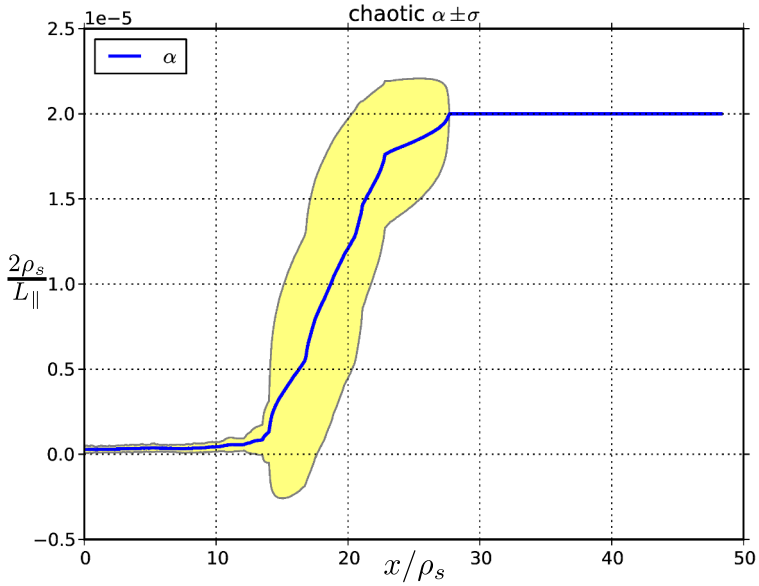

(b) The flux-surface averaged α as a function of the radial position with its rms values superimposed.

Figure 2: 4

To fix the parameters used in this study we adopt an NSTX-like geometry, with minor radius = 68 cm, plasma radius = 60 cm, external coil size =10 cm, R_0 = 85 cm, a_1 =-.01, and consider $I_{ext}/I_p = \epsilon = 0, .1, .2, .3$. We use the map to fix $\alpha(x, y)$ for the duration of the run.

From a macroscopic point of view, one of the effects of the magnetic field chaos is to broaden the transition between closed field lines and open field lines, which appears in an axisymmetric system as a jump in the connection length $L_\parallel$. In order to distinguish the effect of the spatial fluctuations of $L_\parallel$ in a chaotic SOL field from the effect of the broadening of the transition, it is interesting to consider a model in which the chaotic inverse connection length is averaged over an unperturbed flux-surface. We will refer to this case as the "smooth alpha" case, as illustrated in figure 2b.

2.4 Equilibrium

We are interested in characterizing intermittency and global profile sensitivity as a function of the RMP amplitude. Since we will be driving turbulence by introducing a particle source S_n on the core edge of the simulation, it is useful to consider how to select S_n in our model.

The primary density sink in our system is loss through the divertor sheaths (the αn term). If we account for the nonlinear terms through an anomalous diffusivity D_a and assume a source localized at the boundary of the simulation and of the form $S_n = S_0\,\Theta(x_\star - x)$, the profile of the average density will take the form

$$n(x) = n_0 e^{-x\sqrt{\frac{\alpha}{D_a}}} \text{ for } x > x_\star, \tag{6}$$

where $S_0 = 2n_0$. This simple result reflects the fact that the source must roughly balance the dominant sink, represented by the αn term in the density equation.

Note that without a particle source the equations are invariant under a change in the global background density, $n \to n + n_0$. The source strength thus has the effect of setting the background density for given D_a.

3 Numerical Simulations

We use the BOUT++([15, 45, 14]) framework to discretize and evolve equation (1). Specifically, a local polynomial approximation is used to compute derivatives along the x coordinate and pseudo-spectral methods are used to compute derivatives along the y coordinate, and a CVODE([10]) ode solver is used to advance the fields in time. To assess the reliability of our numerical tools we verify the linear dispersion relation in section(3.1.1) as well as verify that nonlinear analytic predictions favorably compare to the single blob dynamics of two other codes ([33], [20]) in section (3.1.2), and finally match published SOL width values [3] in section (3.1.3).

3.1 Verification

3.1.1 Linear Verification

We compare the growth rate of the SOL interchange mode as deduced from a simulation of a linearized version of equation (1) with the analytically derived growth rate γ. For the numerical calculation, several γ^{-1} time increments may be required to converge on the solution, unless one sets the initial condition such that u, ϕ correspond to an eigenvector of the linearized version of equation (1). Expanding equation (1) to the lowest order in ϕ, u, n, setting $D_\varpi = D_n$, and dropping parallel dissipation in the density equation yields the analytic result

$$\gamma = -\frac{\left(\alpha + 2Dk_\perp^4\right)}{2k_\perp^2} + \sqrt{\left(\frac{\alpha}{2k_\perp^2}\right)^2 + \frac{\beta}{\ell_n}}. \tag{7}$$

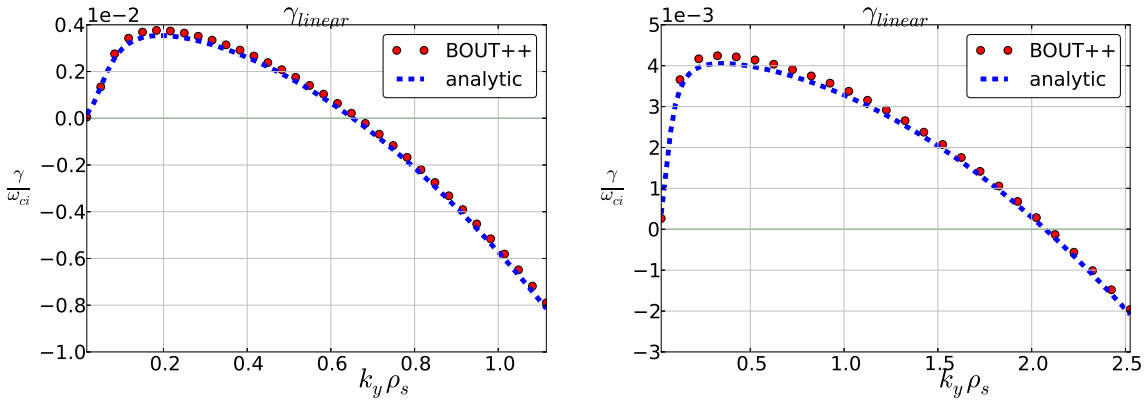

Figure 3: Growth rate γ as a function of the poloidal wavenumber k_y, where $D = \mu = 1 \times 10^{-2}$ and 1×10^{-3} on left and right charts respectively, $\beta = 6 \times 10^{-4}$, $\alpha = 3 \times 10^{-5}$. Good agreement between analytic theory and BOUT++ results is observed.

3.1.2 Single blob dynamics

Comparing numerical solutions of single blob propagation with published results presented by Garcia et al. (2006) ([20]) shows good agreement. The simulations used initial and boundary conditions as shown in Table (1). By design, the simulation domain was large enough to keep the blob sufficiently far away from the boundaries for the duration of the run. In particular, the size of the domain is such that changing boundary conditions between Dirichlet ($n_{x\ boundary} = 0$), and Neumann ($\partial_x n_{x\ boundary} = 0$), only weakly affects the history of the leading moments describing the blob.

Parameter	Value
N_x	1056
N_y	1024
L_x	60
L_y	40
$n(t=0)$	$e^{\frac{(x^2+y^2)}{2}}$
$u(t=0)$	0
BC_x	$\partial_x u = \partial_x n = 0$
BC_y	*periodic*
Ra	$10^{2,4,6}$

Table 1: Numerical Blob Parameters

Comparing the evolution of the center of mass,its velocity as well as the maximum amplitude of the density in the blob shows consistent agreement between BOUT++ generated results and those presented by E .Garcia et al. (2006) as well recent work by C. Michoski [33] and A. Hakim [23].

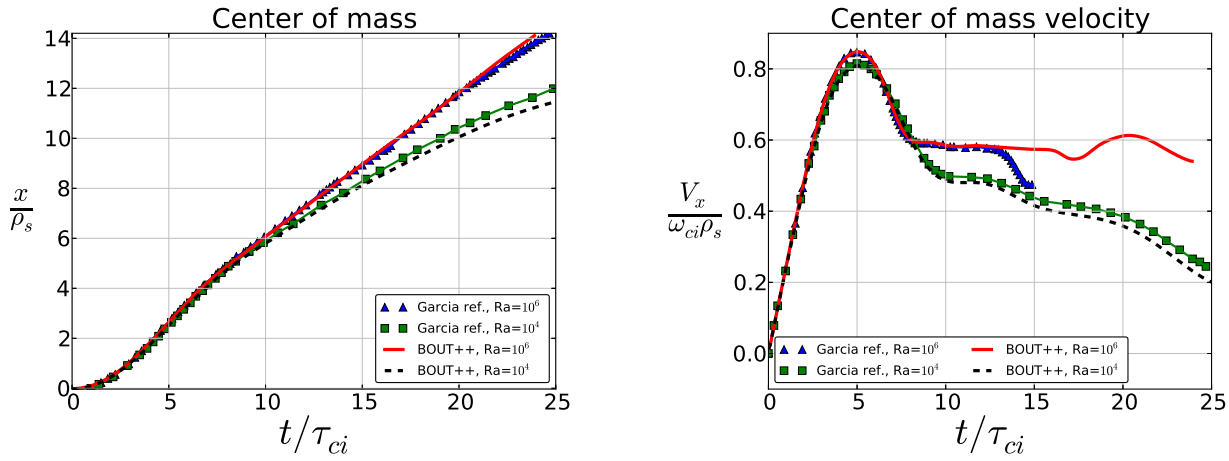

Figure 4: A few scalar blob trajectories are considered. Close agreement is seen with E. Garcia [20], here we run case with Rayleigh number 10^4 and 10^6.

3.1.3 Saturated turbulence

As an additional verification test we considered flux-driven, many-blob interchange turbulence as described by A.Y.Aydemir [3]. To clarify, with this test, as with single blob simulations, we use equation (1), but with a nonzero density source term, S_n, and with radial boundary conditions that allow the profile to relax. Except for having a constant value of α the simulation setup here is similar to ones described in section (3.3). We fit a profile of the form $n = n_0 \exp(-x/\lambda_{SOL})$, to observed flux-surface averaged density values and compare values of λ_{SOL} to published results. Specifically with β/α fixed at 5, while not shown here, we see excellent agreement of λ_{SOL} with results present by A.Y.Aydemir [3] across a wide range of parameters.

3.2 Effect of field-line chaos on a single blob

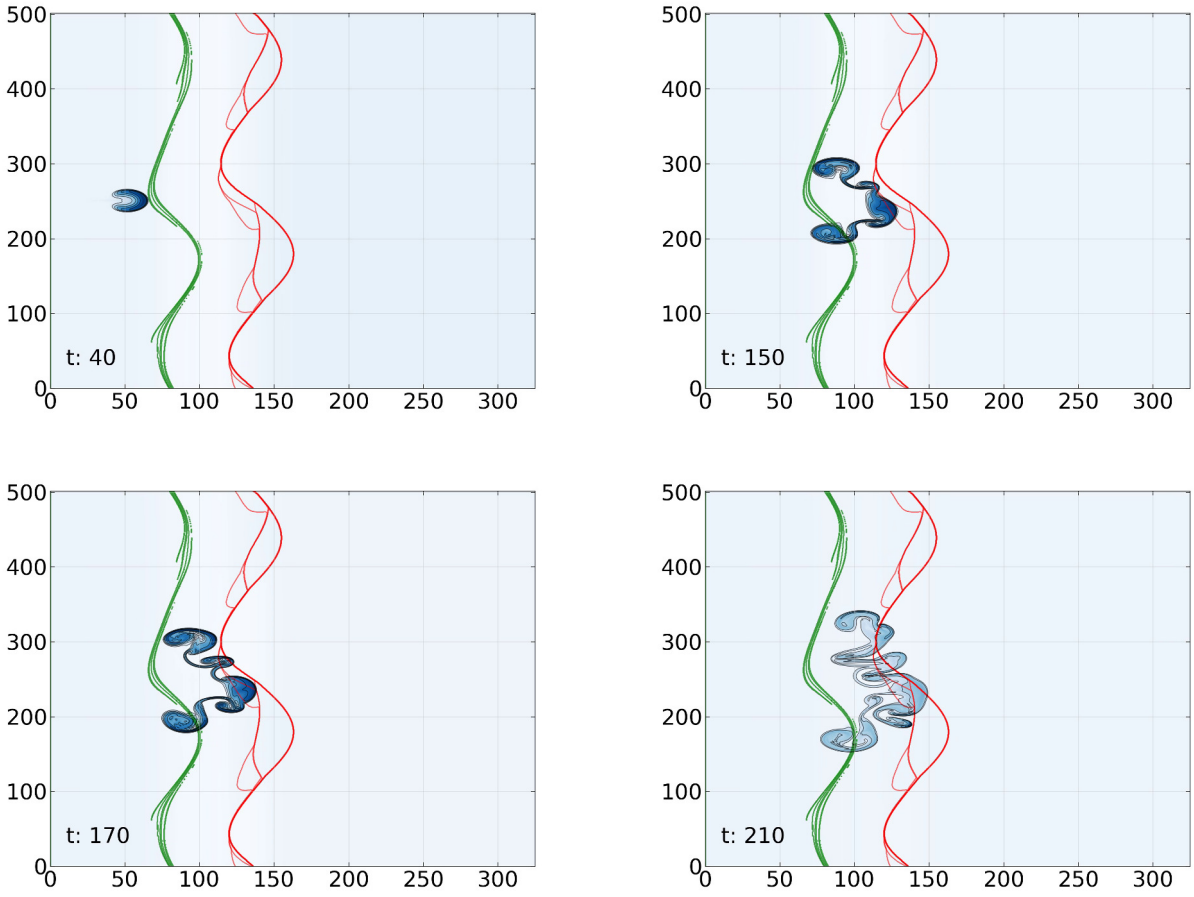

Figure 5: Evolution of a density blob with Rayleigh number = 10^4. The pictured blob encounters a region pierced by chaotic field-lines , demarked here by two equidistant curves. The structure quickly loses symmetry as it propagates radially outward.

In contrast to cases where α is a constant value or is simplified by averaging over a flux-surface, blobs will quickly lose symmetry when propagating through a region with chaotic α as pictured in figure (5). Fine fractal structures of the Poincaré map are not immediately apparent in the single blob response, however saturated many-blob turbulence is a more appropriate framework to evaluate what if any impact field-line chaos will have on the overall transport and the width of the SOL.

3.3 Effect of field-line chaos on saturated turbulence and mean blob size

In this section we are interested in examining the effect of field-line chaos on the SOL. Rather than focus on individual blobs we probe the changes in the mean blob behavior as we consider three scenarios: *a)* chaotic, *b)* smooth, and *c)* unperturbed flux surfaces.

The parameter space of parallel dissipation, diffusion, and source strength values is large and we opt to fix key parameters to be consistent with an NSTX tokamak configuration [43], with $\alpha_{max} = 3.0 \times 10^{-3}$, $\beta = 1.0 \times 10^{-2}$, $D_n = D_\omega = 1.0 \times 10^{-2}$. Typical mesh size is $N_x \times N_y$ = 1024x512, the simulation domain

represents a quarter of a full torus, and typical radial range is $L_x \approx 300\rho_s$. The large radial range, while not representative of the physical size of the SOL, is useful in fitting density scaling parameters, see section 3.4.

Simulations are initialized with a smooth density profile that gently peaks at the core edge and a small driving source term, S_n, as described in section (2.4). We use simple boundary conditions, $\partial_x n \approx 0$ and $u = 0$ on both radial boundaries, that allows the entire density profile to adjust as needed to settle on a turbulent equilibrium profile. Additionally we fix the potential, $\phi = 0$, on the inner radial boundary to ensure that radial particle flux is solely set by the source, S_n.

We can better interpret the many-blob turbulence results in terms of single blob theory by extracting mean blob behavior. To this end we consider fluctuations in the radial convective particle flux,

$$\Gamma_x = \Gamma_{E\times B,x}(x, y, t) = -n\partial_y \phi, \tag{8}$$

and employ spatial spectral analysis and radially resolved auto-correlation analysis to infer the mean length scales of the saturated interchange turbulence present in our system. Specifically we considered the auto-correlation along the poloidal coordinate of the particle flux $\Gamma_x(x, y, t)$ at some fixed point x. We extract the mean periodic scale length and the smallest non-periodic statistically significant length scale, we refer to these lengths as λ_{blob} and δ_{small} respectively.

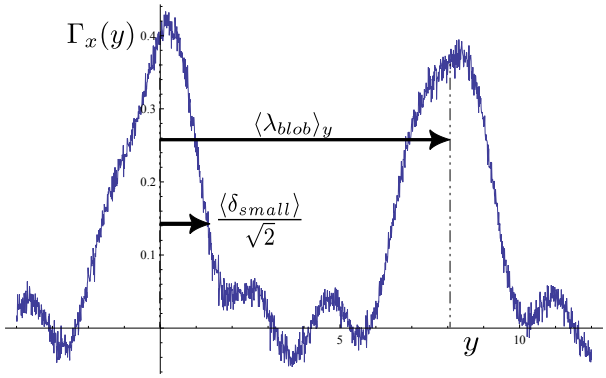

(a) A hypothetical $\Gamma_x(y)$ at a fixed x

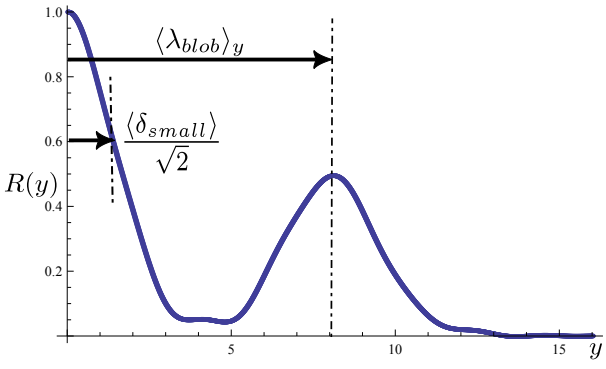

(b) Autocorrelation reveals the relevant length scales

Figure 6: The mean size of the smallest reoccurring feature in y can be shown to be $\langle\delta_{small}\rangle_y \approx \sqrt{2}\sigma$, where σ is determined by a least-squares fit of a Gaussian, $e^{-\frac{y^2}{2\sigma^2}}$, around the central peak of $R(y)$

In processing simulation results of flux Γ_x, blobs will show up as isolated, generally radially outward propagating local maxima in $\Gamma_x - \langle\Gamma_x\rangle_y$. Consider figure (7), where a snapshot of the particle flux at a point in time is presented (7a), and more detailed figures follow, where $E \times B$ velocity fields are overlaid to give a sense of flow direction.

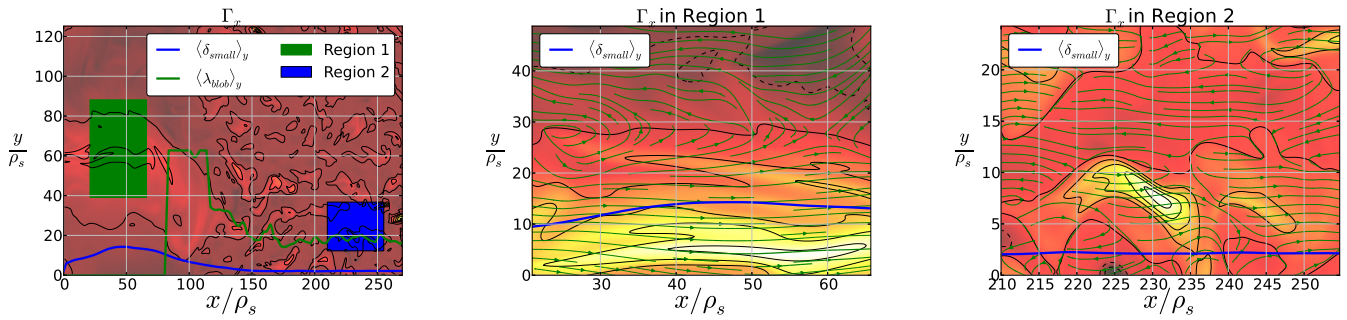

(a) snapshot of Γ_x (b) Region 2 with $V_{E\times B}$ flow detail (c) Region 1 with $V_{E\times B}$ flow detail

Figure 7: Details of radially outward particle flux Γ_x with average blob size $\langle\delta_{blob}\rangle_y$. The difference in the values of the α parameter is reflected in the size of the blobs in the two closeups images.

In figure (8) we superimpose the spectral density of fluctuations, analytic predictions, and scale lengths obtained from auto-correlation onto a single image that summarizes all important length scales as a function of x. The intensity of the filled contour plot is proportional to a time averaged value of the spectral density. The spectral density is re-normalized at each radial location to clearly display the spectral density for all x, even as the amplitude of fluctuations decays exponentially in the radially outward direction. See appendix (A) for additional details on auto-correlation analysis and background information on spectral density.

Wavenumbers associated with a few analytically predicted length scales are overlaid in figure(8). These expressions can be extracted from equation (1) using term balancing, see A. Aydemir [3]. As seen in figure(8) the blob size, for the parameters considered, stays close to inertial scale length, and the mean size of the finer structures, δ_{small}, stays close to the most unstable linear scale. Inertial scale is the length scale at which both inertia and parallel momentum losses are comparable with the curvature drive. Relating operators in the momentum equation (1a) to some typical blob size a we write

$$\left(\frac{\phi}{a^2}\right)^2 + \frac{\beta}{a} - \alpha\phi + \frac{D_\omega\phi}{a^4} = 0, \tag{9}$$

the desired length scale a_m must then satisfy the following relations,

$$\left(\frac{\phi}{a_m^2}\right)^2 \approx \frac{\beta}{a_m}, \qquad \alpha\phi \approx \frac{\beta}{a_m}. \tag{10}$$

It follows easily that equation (10) is satisfied when $a_m^5 = \beta/\alpha^2$. Additionally we observe that spectral density appears to taper off below the parallel upper limit k_α. Modes below this value are dominated by end-losses, and typically lose mass and decohere quickly. We can derive this length scale similarly to the preceding example. Rewriting operators in the continuity equation in terms of some scale length a_α yields

$$\frac{D_n}{a^2} + \frac{\phi}{a^2} + \alpha = 0. \tag{11}$$

When parallel particle losses roughly balance particle flux in equation (11), and curvature drive is comparable to parallel momentum losses in equation (9) the implied length scale a_α must satisfy

$$\frac{\phi}{a_\alpha^2} + \alpha \approx 0 \qquad \alpha\phi \approx \frac{\beta}{a_\alpha}. \tag{12}$$

Again it straightforward to show that

$$a_\alpha^3 = \frac{\beta}{\alpha^2}. \tag{13}$$

We also note that the curvature drive term gets bigger as a gets smaller, therefore a_α must be the smallest length scale at which parallel dissipation can be comparable to curvature drive. In k-space this will correspond to some upper wavenumber limit, where $k_\alpha = \sqrt{2}/a_\alpha$, when we correctly relate periodic and spatially localized/non-periodic length scales.[1]

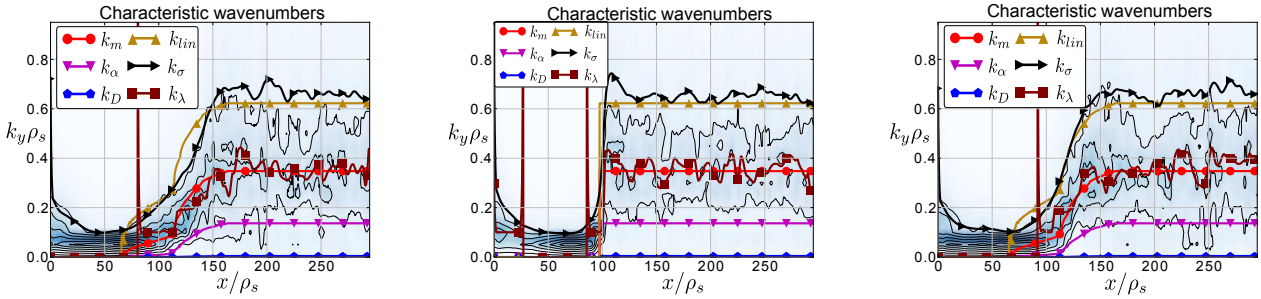

(a) chaotic α (b) unperturbed α (c) smooth α

Parameter	Value
inertial lower limit:	$k_m = \frac{\sqrt{2}}{(\beta/\alpha^2)^{1/5}}$
diffusive upper limit:	$k_{D_n} = \frac{\sqrt{2}(\alpha D_n)}{\beta}$
parallel upper limit:	$k_\alpha = \frac{\sqrt{2}}{(\beta/\alpha^2)^{1/3}}$
viscous lower limit:	$k_{D_\omega} = \frac{\sqrt{2}}{(D_\omega/\alpha)^{1/4}}$
linear scale:	$k_{lin}(\gamma_{max}) \approx \left(\frac{\alpha}{D_n}\right)^{1/4}$
mean detected blob size:	$k_{\lambda_{blob}} \approx \frac{2\pi}{\lambda_{blob}}$
width of central peak of R_{Γ_x}:	$k_\sigma = \frac{\sqrt{2}}{\delta_{small}}$

Figure 8: Wavenumbers or length scales present in Γ_x fluctuations indicate that the inertial scale length, with a corresponding wavenumber k_m, provides a good estimate of the mean blob size. Additionally we observe that the smallest significant scale length corresponds to a length scale for which we expect the linear growth rate γ to peak, where $k = k_{lin} \approx (\alpha/D_n)^{1/4}$. The nature of the abrupt jump in α field is clear in figure (b), the differences between smooth and chaotic cases is not immediately clear. As indicated by the black curve significant blob break-up is observed in all three cases.

We can see that the mean blob size does not seem to be strongly affected by the fractal character of the α field but does seem to respond quickly to the local-in-x variations in the y-averaged parallel connection length, as indicated in figure (8) with curve labeled k_λ. We expect the smallest observed, δ_{small} sized, fluctuation and its corresponding wavenumber k_σ, to be most sensitive to the chaotic nature of the field-lines. While generally k_σ closely tracks the most unstable linear wavenumber, $k_{lin} \approx (\alpha/D_n)^{(1/4)}$, in the region where α transitions from 0 to α_{max} wavenumber k_σ seems to be consistently smaller in the case with chaotic

[1]To correctly associate a non-periodic or spatially localized length scale with a wavenumber we consider the auto-correlation function of the two signal types. Consider an auto-correlation function of a sine wave, and an auto-correlation function of some non-periodic signal, call them R_{sine} and $R_{noperiod}$ respectively. Note that the non-periodic signal will still have characteristic length scales. As reviewed in figure(6) the central peak of the auto-correlation function $R_{noperiod}$ will have a standard deviation of $\sqrt{2}\sigma_x$, where $2\sigma_x$ can be equated with a diameter a. The auto-correlation of a periodic signal will be another periodic signal with the same period as the input signal. Using least-squares we can fit a Gaussian around the central peak of R_{sine} to see that it has a standard deviation of $1/k$, it follows that

$$\frac{1}{k} = \sqrt{2}\sigma_x = \sqrt{2}\frac{a}{2} \Rightarrow k = \frac{\sqrt{2}}{a}. \tag{14}$$

field-lines than in the case with the smooth simplification pictured in figure (8c). The simplest explanation for this observed difference is that highly spatially localized variations in α, are essentially ignored by the smallest coherent flux structures, lowering the effective average value of α which determines the unstable linear scale length. In relation to the Poincaré magnetic field line map this observation implies that highly localized escape basins, while allowing individual particles to escape toroidal confinement quickly, do not qualitatively change the character of the average radially propagating coherent structure.

We can see that the mean blob size does not seem to be strongly affected by the fractal character of the α field but does seem to respond quickly to the local-in-x variations in the y-averaged parallel connection length. For many machines inertial blobs can be expected to be several multiples of the ion-acoustic gyro-radius,

$$a_m = (\frac{(2\pi q(R))^2 R}{\rho_s})^{1/5}\rho_s \approx (2-3)\rho_s.$$

The simple approach that arrives on a set of characteristic length scales on the non-vanishing α end of the simulation domain neglects zonal flows which are seen to dominate the $\alpha = 0$ end of the simulation domain, and are in fact present throughout. Zonal flows are important in setting the blob creation rate and have a non-trivial interaction with radial electric field shear, see [43].

3.4 Profile characterization

We fit a simple profile to our simulation results where the gradient of $\log(n_{fit})$ along x smoothly changes from some λ_{core} to another λ_{SOL} with some transition region of width w_n linking inner and outer regions,

$$\partial_x \log(n) = A + B \arctan\left(\frac{x - x_0}{\Delta x}\right) = 0, \tag{16a}$$

$$A = \frac{\lambda_{core} + \lambda_{SOL}}{2}, \tag{16b}$$

$$B = \frac{\lambda_{SOL} - \lambda_{core}}{\pi}. \tag{16c}$$

Integrating equation(16) yields a longer analytic expression and introduces a constant of integration. We minimize the difference of the squares to compute $\Delta x, \lambda_{SOL}, \lambda_{core}$ and some constant of integration. We find a region of width w_n where the derivative of n_{ave} is within one standard deviation of maximum value, this is the value reported on the y-axis in Figure(10).

The width of the density shoulder, w_n, appears to scale linearly with the width of the α transition, w_α, chaotic or smooth. The density scale length λ_{SOL} in the far SOL does not have a strong dependence on the character of the α transition. This observation combined with blob size measurements in section (3.3) indicates that both globally averaged profiles and the mean blob-size, are consistently insensitive to the finer details of how α transitions from 0 to some maximum α_{max}. In the next section rather than simply compute the average profiles and blobs sizes we examine the distribution of fluctuations in greater detail. A. Aydemir [3] proposed modeling transport in the SOL with a collection of blobs, sized at roughly the most unstable linear scale length at birth that propagate radially outward. Our observations are consistent with this approach and explicitly verify that inertial blobs dominate convective particle flux fluctuations.

3.5 Statistics of density and convective flux fluctuations in the SOL

Single point measurements of density fluctuations are possibly the most common way to detect large bursty events in the SOL and a large body of experimental and theoretical work surrounds this diagnostic in the context of blobs and many-blob turbulence, [19, 49, 28]. One difference between data-gathering permitted by numerical work over experiment is that rather than being limited to several locations where probe data

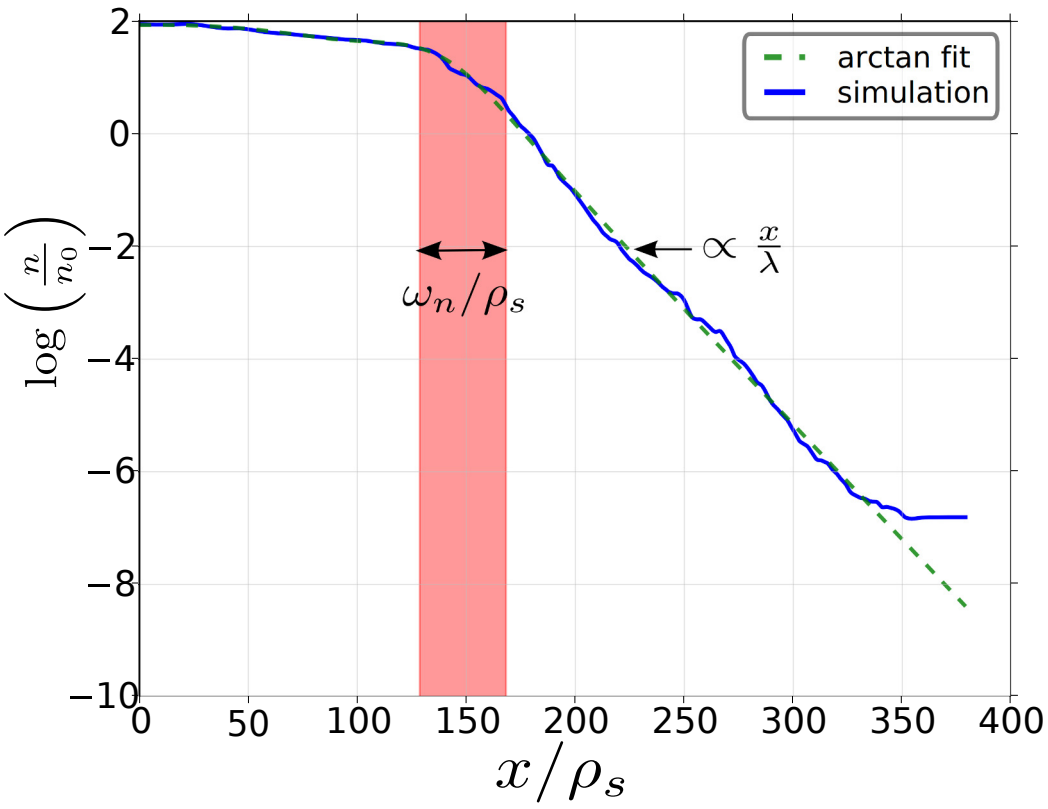

Figure 9: Typical n_{ave} profile (solid) with the detected shoulder region shaded, along with a fit of a smoothly connected two λ profile model (dashed).

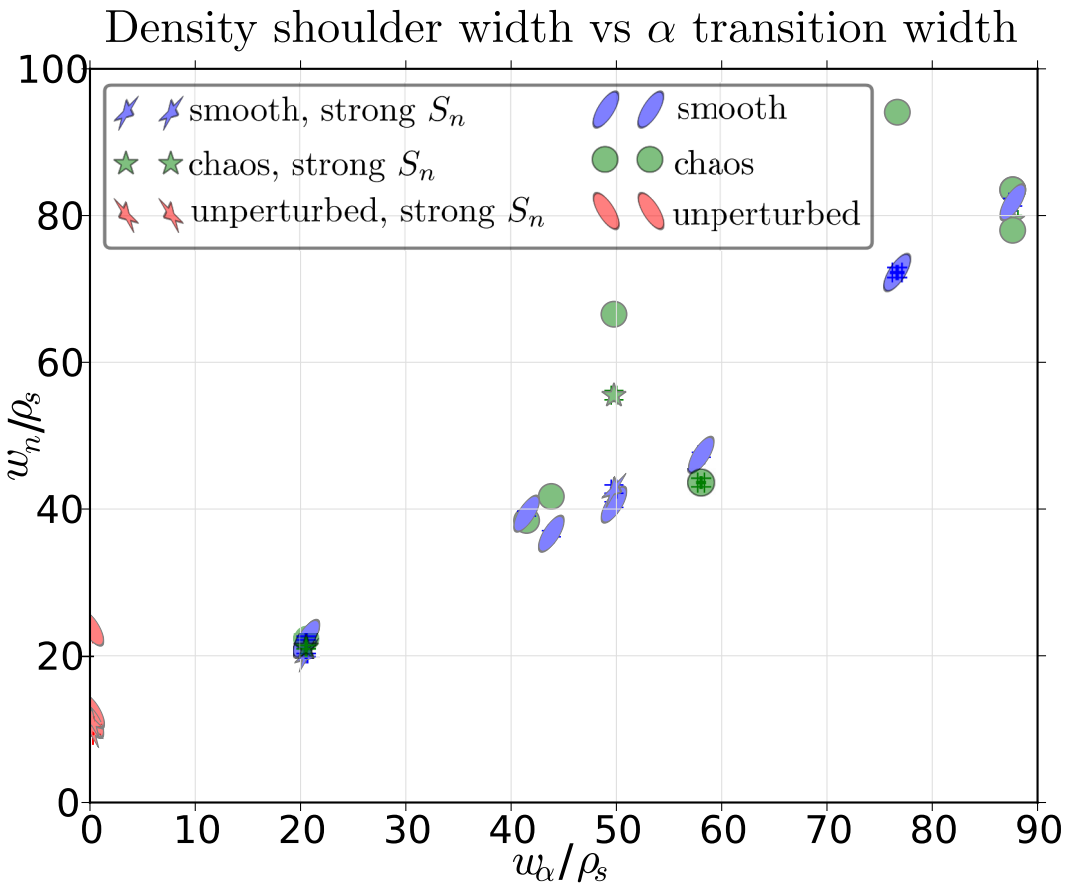

Figure 10: While for the chaotic cases we see more large deviations from a simple linear relationship between the width of the α mixing length and the width of the n_{ave} shoulder, it seem to lie within the same scaling range as the smooth α set of values.

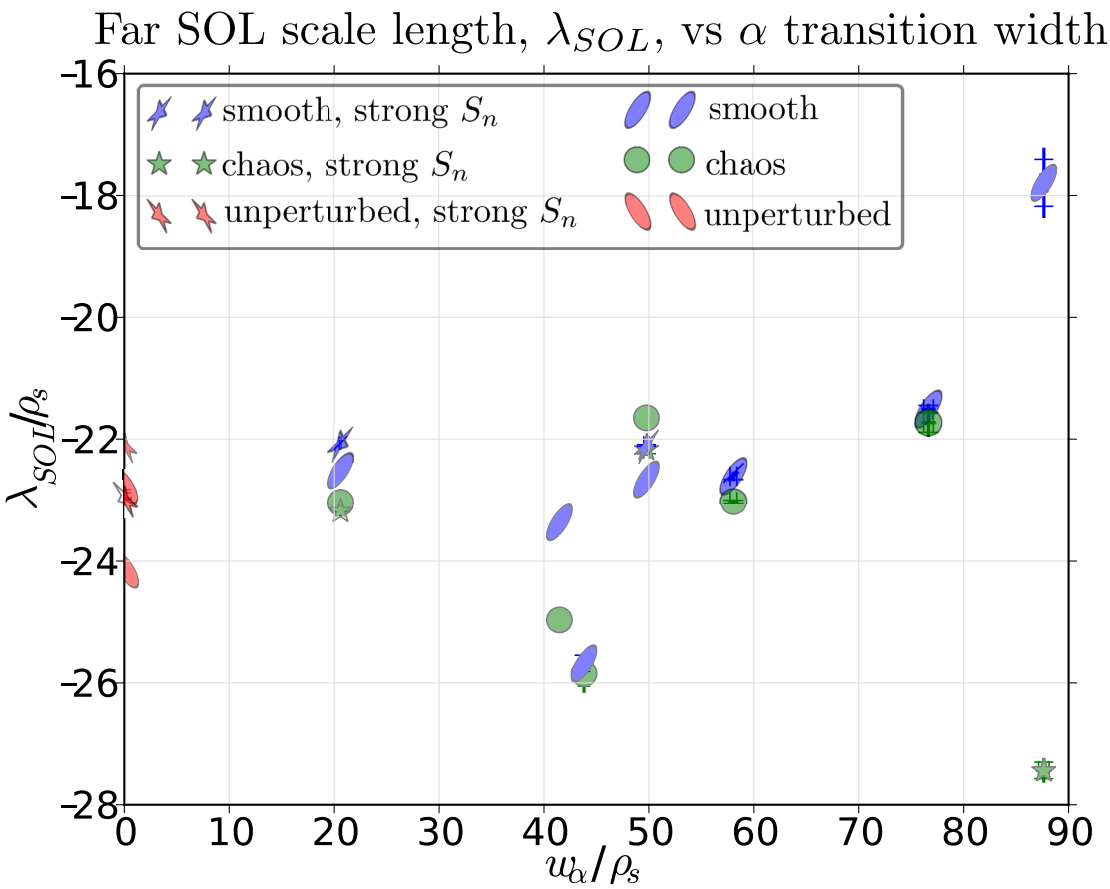

Figure 11: Far SOL width, λ, does not show any clear dependence on the chaotic properties of the α profile

is available we can consider fluctuations across the entire computational domain. Additionally we can consider fluctuations in the radial component of the particle flux, Γ_x. This is a simple way to limit our attention to density fluctuations that have a nonzero radial velocity component.

To examine how different distributions deviate from an idealized Gaussian we can normalize the bins enumerating the number of counts of a particular flux amplitude with the Γ_{rms} specific to that numerical experiment. With this approach all Gaussian distributions, regardless of their individual Γ_{rms} values would sit on a single curve.

3.6 Particle flux

One quantity we are ultimately interested in, that our model can provide, is the maximum particle flux. We can consider a histogram of radial particle flux and density fluctuations; an efficient way to examine the difference in the number of high particle flux events between the considered cases.

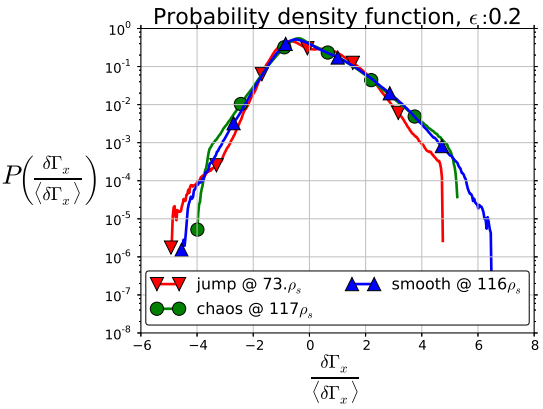

(a) Histogram of normalized convective particle flux Γ_x fluctuations. The manner in which chaotic and smooth α distributions deviate from a Gaussian is similar.

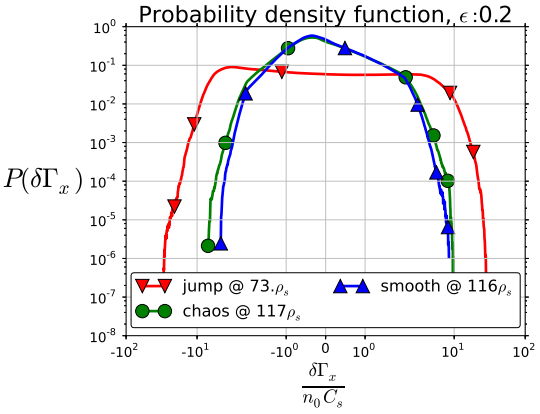

(b) Histogram of unnormalized Γ_x fluctuations. We see the unperturbed case has a strongly bimodal distribution and largest absolute deviations from its mean value.

Figure 12: Here we examine the distribution of convective particle flux fluctuations, near the maximum in the density gradient, in practice this is usually just outside the separatrix. As seen in panel(b), it appears that a chaotic RMP-like rearrangement shows little affect on the frequency of high flux events, as compared to the smooth case. The magnetic perturbation is $I_{ext}/I_p = .2$ for this case.

Looking further away from the shoulder region we see that all three cases appear to have a very similar distribution of fluctuations.

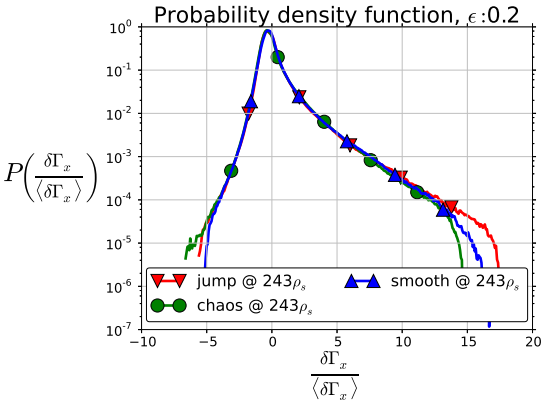

(a) Histogram of normalized convective particle flux Γ_x fluctuations. The three distributions appear essentially the same far enough from the separatrix.

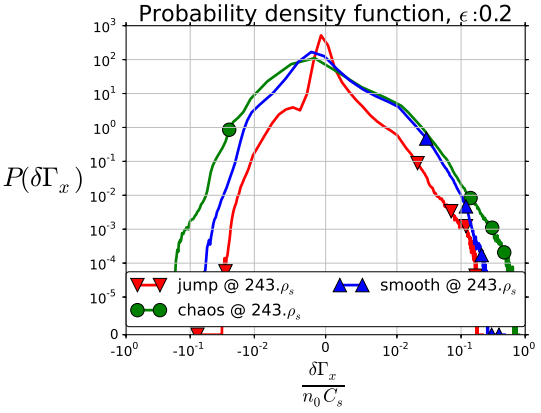

(b) Histogram of unnormalized Γ_x fluctuations. The significantly lower values of flux fluctuation for the abruptly changing α can be reconciled by noticing, that for a given position outside the separatix, the density field has experienced more parallel dissipation as it moved radially outward, due to lack of intermediate values of α between 0 and α_{max}.

Figure 13: The distribution of convective particle flux fluctuations far from the separatrix.

Histograms of density fluctuations tell a similar story, with little difference between smooth and chaotic α cases.

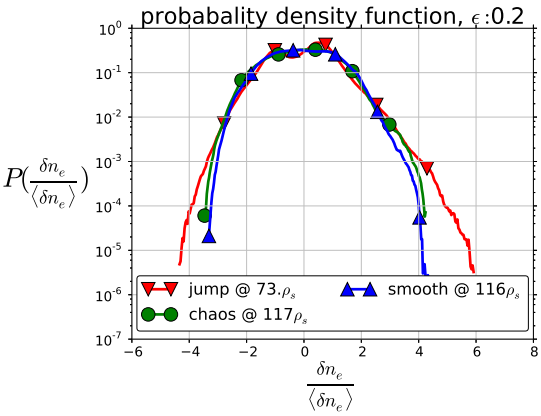

(a) Probability density function (PDF) of density fluctuation near $(\partial_x n_e)_{max}$

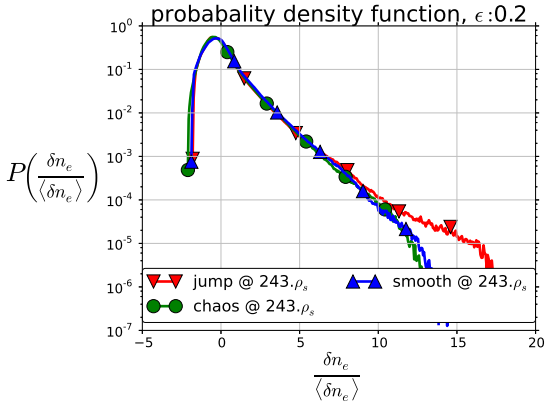

(b) Further away from the separatrix the probability distributions collapse onto a single curve characterized by some positive skewness - indicative of intermittent positive density events.

Figure 14: The case with an unperturbed α, in red, shows the highest relative number of high density events, and has the most clearly bimodal (two-peak) distribution among the considered cases, implying a region where blobs and holes tend to have a relatively narrow range of typical respective values, as compared to the other two cases. When fluctuation counts are normalized as described, the differences between smoothly varying and chaotic α fields are small and subtle. Only the $\epsilon = .2$ case is illustrated here, however other values of ϵ yield qualitatively similar results.

While there are no strong differences between the statistics from smoothly varying and chaotic α simulations, in either the overall shape of the fluctuation distribution or maximum values of particle flux, fluctuations associated with an abruptly changing α show a significantly different distribution that is strongly bi-modal and exhibits a greater number of high intensity events. This observation is qualitatively consistent with section (3.3) where we note that for the case of abruptly changing α, immediately outside the separatrix, the observed blobs, as inferred from auto-correlation of Γ_x, are smaller and therefore can be expected to travel faster and generate sharper wave-fronts relative to larger blobs. Whatever initial differences may have been observed between the three distributions immediately outside the separatrix mostly disappear when the point of observation moves $1/2$ of the total radial domain size away from the separatrix, as pictured in figure (13).

A quantitative treatment examining a couple of leading moments of the density PDF beyond the simple mean and standard deviation, specifically skewness and kurtosis, can be used to further quantify intermittency and identify the blob birth zones. However, this analysis reveals little systematic difference between chaotic and smooth α fields. Moreover one could argue that reducing the maximum particle flux is the most important feature we are interested in and this is well quantified by the observed range in the histograms presented in figures (12) and (13).

4 Conclusion

We have analyzed turbulent steady state density profiles in the SOL with a simple electrostatic interchange edge turbulence model applicable to a broad range of devices. Specifically we considered how changing the character of the transition between zero and strong sheath coupling changes the character of the steady state profiles. We found that characterization of the scrape off layer by the common metric of an e-folding density scaling length remains largely unchanged in far scrape-off layer. Closer to the separatrix, in the

transitional zone between $\alpha = 0$ and α_{max}, the mean density profile has a local maximum in the density gradient whose width , w_n,roughly mirrors the width of the α transition, w_α. Both flux-surface averaged and chaotic cases show similar so-called shoulder widths w_n. From a practical standpoint this implies that the fine details of the chaotic structure of α are not necessary to create useful empirical models that relate state-steady profile shape and persistent magnetic chaos.

We observe that radial transport in this SOL model, considered in a simple slab geometry, is dominated by blobs of a specific size, regardless of the nature of the interface between the closed flux surfaces and the far SOL. Furthermore, the observed density scaling length is only weakly affected by the state of the plasma at the interface where blob birth takes place, once a sheath-connected blob is established. While the introduction of a chaotic interface, where externally introduced magnetic field deforms or even breaks the last closed flux surface, does encourage blob and hole formation over a wider radial region, the same effect can be achieved by running the numerical experiment with smoothly varying connection lengths lacking any chaotic features.

We compute probability density functions (PDFs) for the observed density and convective radial flux fluctuations to see that a chaotic magnetic field will generally produce fluctuation statics that differ little from the smoothly varying case. This again suggest that assuming a smoothly varying parallel connection length between just inside separatrix and the far SOL is a sufficient description when dealing with physics that is otherwise well characterized by a simple 2D electrostatic model. Additionally as seen in Figure(12) application of chaotic magnetic fields does in fact lower the maximum particle flux that can be expected, suggesting that RMPs may be helpful in limiting divertor damage and impurity contamination.

Ongoing work will extend the presented work by including electron temperature in the system of equations, will include the full form of the $\langle \nabla_\parallel j_\parallel \rangle$ and $n\langle \nabla_\parallel v_\parallel \rangle$ terms rather than the linearized version as done here, and will recognize the presence of a core-facing region that is better described with a Hasegawa-Wakatani system of equations rather than a sheath coupled, interchange dominated system. In the flute approximation we expect to see the fields making up our system to vary weakly along field lines, in a two-dimensional model this should manifest itself as strong non-local coupling at every point to every other point intersected by the same field line, or perhaps approximated by an anomalous diffusion coefficient in smooth regions, neither is implemented in this work. The most straightforward solution to this geometric issue is to include the parallel dimension in the simulation domain which we are currently investigating.

A autocorrelation

We consider auto-correlation along the poloidal coordinate of particle flux $\Gamma_x(x, y, t)$, at some fixed point x. We define auto-correlation as the usual measure of similarity of a signal with itself shifted by some poloidal displacement,

As shown in figure (6) at least two characteristic length scales can be extracted: the width of the central peak of R, refered to as $\langle\delta\rangle_y$ and some primary period $\langle\lambda_{blob}\rangle_y$, or in shorthand notation δ_{small} and λ_{blob}. We anticipate that λ_{blob} is a wavelength that can be related to mean blob size, and δ_{small} is simply the smallest observed coherent convective density flux structure that is statistically significant. In the subsequent discussion we show that δ_{small} and λ_{blob} agree well with simple analytic predictions of dominant linear instability scale length and blob size, respectively.

In addition to computing the auto-correlations of Γ_x, we can consider a discrete Fourier transform of Γ_x, specifically

$$\widetilde{\Gamma}_x = \widetilde{\Gamma}_x(x, k_y, t) = \int_0^{L_y} dy e^{-i2\pi k_y y}\, \Gamma_x. \tag{17}$$

We can go on to compute a time average of the spectral density $P(x, k_y, t)$, where

$$P(x, k_y) = \overline{P(x, k_y, t)} = \frac{1}{(t_1 - t_0)} \int_{t_0}^{t_1} dt\, \widetilde{\Gamma}_x \widetilde{\Gamma}_x^{\star}. \tag{18}$$

Note that this is simply the absolute value of the Fourier transform $\widetilde{\Gamma}_x$, squared and time averaged, or equivalently a Fourier transform of the auto-correlation $R(x, k_y)$ time averaged. Local maxima of $P(x, k_y)$ along k_y indicate dominant wavenumbers; important periodic features along the poloidal direction.

B length scales discussion

To illustrate consider the inertial scale length, where auto-correlation analysis indicates where the vast majority of the blobs we detect reside. We relate operators in our equation to some characteristic spatial scale length a,

$$(\partial_t + V_E \cdot \nabla) \rightarrow \frac{\phi}{a^2} \qquad \partial_y \rightarrow \frac{1}{a} \qquad \nabla^2 \rightarrow -\frac{1}{a^2}. \tag{19}$$

We can tag the inertial term in equation (1) by adding a nominal coefficient A_i. This simple bookkeeping trick will allow us to examine the scale lengths in the inertially dominated limit, as

$$-A_i \left(\frac{\phi}{a^2}\right)^2 + \frac{\beta}{a} - \alpha\phi + \frac{D_\varpi \phi}{a^4} = 0, \tag{20a}$$

$$\frac{D_n}{a^2} + \frac{\phi}{a^2} + \alpha = 0. \tag{20b}$$

Solving for ϕ in equation (20a), substituting the result into (20b), yields an equation that will let us examine length scales associated with the different physics included in this model. Expanding the final equation in the limit $A_i \gg \alpha, \beta, D_\varpi$, and D_n will give us some idea of the spatial scales required to satisfy equation (21) when inertia dominates:

$$\frac{\sqrt{a\beta}\sqrt{\frac{1}{A_i}}}{a} - \frac{a^2\alpha}{2A_i} + \mathcal{O}[\frac{1}{A_i}]^0 = 0. \tag{21}$$

Setting A_i to 1, we solve for a, denoting it a_m, as

$$a_m^5 = \frac{\beta}{\alpha^2}. \tag{22}$$

By inspection from equation (20) we see that in the limit $a \to \infty$ inertia can be neglected. In other words a_m must be some lower limit, so we can ignore inertia when $a \gg a_m$.

In addition, other relevant scales can be derived, as discussed in [3, 50, 12]. For reference: $k_m = \frac{\sqrt{2}}{(\beta/\alpha^2)^{1/5}}$ sets a lower limit on k_y for which inertia matters, while $k_{D_\omega} = \frac{\sqrt{2}}{(D_\omega/\alpha)^{1/4}}$, sets an lower limit on k_y for which viscous diffusion matters, $k_D = \frac{\sqrt{2}(\alpha D_n)}{\beta}$ sets an upper k_y for which particle diffusion matters, and $k_\alpha = \frac{\sqrt{2}}{(\beta/\alpha^2)^{1/3}}$ sets an upper k_y where parallel particle dissipation matters.

References

[1] Justin R. Angus, Sergei I. Krasheninnikov, and Maxim V. Umansky. Effects of parallel electron dynamics on plasma blob transport. Physics of Plasmas, 19(8):082312, Aug 2012.

[2] Justin R. Angus, Maxim V. Umansky, and Sergei I. Krasheninnikov. Effect of Drift Waves on Plasma Blob Dynamics. Physical Review Letters, 108(21):215002, May 2012.

[3] A. Y. Aydemir. Convective transport in the scrape-off layer of tokamaks. Physics of Plasmas, 12(6):062503, 2005.

[4] R Barni and C Riccardi. Advection of long lived density blobs in the turbulent state of a simple magnetized torus plasma. Plasma Physics and Controlled Fusion, 51(8):085010, 2009.

[5] S. Benkadda, T. Dudok de Wit, A. Verga, A. Sen, ASDEX team, and X. Garbet. Characterization of coherent structures in tokamak edge turbulence. Phys. Rev. Lett., 73(25):3403–3406, Dec 1994.

[6] H. L. Berk and G. V. Stupakov. Stability of the gas dynamic trap. Physics of Fluids B: Plasma Physics, 3(2):440, 1991.

[7] N. Bian, S. Benkadda, J.-V. Paulsen, and O. E. Garcia. Blobs and front propagation in the scrape-off layer of magnetic confinement devices. Physics of Plasmas, 10(3):671, 2003.

[8] J. A. Boedo, D. Rudakov, R. Moyer, S. Krasheninnikov, D. Whyte, G. McKee, G. Tynan, M. Schaffer, P. Stangeby, P. West, S. Allen, T. Evans, R. Fonck, E. Hollmann, A. Leonard, A. Mahdavi, G. Porter, M. Tillack, and G. Antar. Transport by intermittent convection in the boundary of the diii-d tokamak. Physics of Plasmas, 8(11):4826–4833, 2001.

[9] L. Chacón. An optimal, parallel, fully implicit Newton–Krylov solver for three-dimensional viscoresistive magnetohydrodynamics. Physics of Plasmas, 15(5):056103, 2008.

[10] S. Cohen and C. Hindmarsh. Cvode, A Stiff/nonstiff Ode Solver In C. Computers in Physics, 10(2):138–143, March 1996.

[11] D. A. D'Ippolito, J. R. Myra, S. I. Krasheninnikov, G. Q. Yu, and A. Yu Pigarov. Blob Transport in the Tokamak Scrape-off-Layer. 95:1–12, 2003.

[12] D. A. D'Ippolito, J. R. Myra, and S. J. Zweben. Convective transport by intermittent blob-filaments: Comparison of theory and experiment. Physics of Plasmas, 18(6):060501, 2011.

[13] J. F. Drake and Thomas M. Antonsen. Nonlinear reduced fluid equations for toroidal plasmas. Physics of Fluids, 27(4):898, 1984.

[14] B Dudson. BOUT ++ Users Manual. Options, pages 1–11, 2007.

[15] B D Dudson, M V Umansky, X Q Xu, P B Snyder, and H R Wilson. BOUT ++ : A framework for parallel plasma fluid simulations. Computer Physics Communications, 180(9):1467–1480, 2009.

[16] Ben Dudson, Sean Farley, and Lois Curfman. Improved Nonlinear Solvers in BOUT++. pages 1–14, 2012.

[17] T. Evans, R. Moyer, P. Thomas, J. Watkins, T. Osborne, J. Boedo, E. Doyle, M. Fenstermacher, K. Finken, R. Groebner, M. Groth, J. Harris, R. La Haye, C. Lasnier, S. Masuzaki, N. Ohyabu, D. Pretty, T. Rhodes, H. Reimerdes, D. Rudakov, M. Schaffer, G. Wang, and L. Zeng. Suppression of Large Edge-Localized Modes in High-Confinement DIII-D Plasmas with a Stochastic Magnetic Boundary. Physical Review Letters, 92(23):235003, June 2004.

[18] O. E. GARCIA. Blob transport in the plasma edge: a review. Plasma and Fusion Research, 4:019–019, 2009.

[19] O. E. Garcia. Stochastic modeling of intermittent scrape-off layer plasma fluctuations. Phys. Rev. Lett., 108:265001, Jun 2012.

[20] O. E. Garcia, N. H. Bian, and W. Fundamenski. Radial interchange motions of plasma filaments. Physics of Plasmas, 13(8):082309, 2006.

[21] O. E. Garcia, V. Naulin, A. H. Nielsen, and J. Juul Rasmussen. Computations of intermittent transport in scrape-off layer plasmas. Phys. Rev. Lett., 92(16):165003, Apr 2004.

[22] Ph Ghendrih, A Grosman, and H Capes. Theoretical and experimental investigations of stochastic boundaries in tokamaks. Plasma Physics and Controlled Fusion, 38(10):1653–1724, 1996.

[23] Ammar Hakim, Greg Hammet, and Eric Shi. High-order discontinuous galerkin solver for (drift/gyro) kinetic simulations of edge plasmas. APS-DPP 2013, November 2013.

[24] T. C. Hender, R. Fitzpatrick, A. W. Morris, P. G. Carolan, R. D. Durst, T. Edlington, J. Ferreira, S. J. Fielding, P. S. Haynes, J. Hugill, I. J. Jenkins, R.. J. La Haye, B. J. Parham, D. C. Robinson, T. N. Todd, M. Valovic, and G. Vayakis. Effect of resonant magnetic perturbations on COMPASS-C tokamak discharges. Nucl. Fusion, 32:2091, 1992.

[25] M. Kotschenreuther, T. Rognlien, and P. Valanju. Implications of convective scrape-off layer transport for fusion reactors with solid and liquid walls. Fusion Engineering and Design, 72(1â“3):169 – 180, 2004. ¡ce:title¿Special Issue on Innovative High-Power Density Concepts for Fusion Plasma Chambers¡/ce:title¿.

[26] S. I. KRASHENINNIKOV, D. A. D'IPPOLITO, and J. R. MYRA. Recent theoretical progress in understanding coherent structures in edge and sol turbulence. Journal of Plasma Physics, 74(05):679–717, 2008.

[27] S.I. Krasheninnikov. On scrape off layer plasma transport. Physics Letters A, 283(5-6):368–370, May 2001.

[28] B Labit, A Diallo, A Fasoli, I Furno, D Iraji, S H Müller, G Plyushchev, M Podestà, F M Poli, P Ricci, C Theiler, and J Horaček. Statistical properties of electrostatic turbulence in toroidal magnetized plasmas. Plasma Physics and Controlled Fusion, 49(12B):B281–B290, December 2007.

[29] B. LaBombard, R. L. Boivin, M. Greenwald, J. Hughes, B. Lipschultz, D. Mossessian, C. S. Pitcher, J. L. Terry, and S. J. Zweben Alcator Group. Particle transport in the scrape-off layer and its relationship to discharge density limit in alcator c-mod. Physics of Plasmas, 8(5):2107–2117, 2001.

[30] R.J. Maqueda, D.P. Stotler, and the NSTX Team. Intermittent divertor filaments in the national spherical torus experiment and their relation to midplane blobs. Nuclear Fusion, 50(7):075002, 2010.

[31] S. McCool, J. Y. Chen, A. J. Wooton, et al. The effect of magnetic perturbations on edge transport in TEXT. J. Nucl. Mater., 176-177:716–720, Dec 1990.

[32] C. Michoski, C. Dawson, E. J. Kubatko, J. J. Westerink, D. Wirasaet, and C. Mirabito. Adaptive hierarchic transformations for dynamically p-enriched slope-limiting over discontinuous galerkin systems of generalized equations. Journal of Computational Physics, 34:8028–8056, December 2011.

[33] C. Michoski, D. Meyerson, T. Isaac, and F. Waelbroeck. Discontinuous galerkin methods for plasma physics in the scrape-off layer of tokamaks. Journal of Computational Physics, submitted.

[34] P. J. Morrison. Magnetic field lines, Hamiltonian dynamics, and nontwist systems. Physics of Plasmas, 7(6):2279, 2000.

[35] J. R. Myra, D. A. D'ippolito, S. I. Krasheninnikov, and G. O. Yu. Convective transport in the scrape-off-layer by nonthermalized spinning blobs. Physics of Plasmas, 11(9):4267 – 4274, 2004.

[36] J. R. Myra, D. A. Russell, and D. A. D'Ippolito. Transport of perpendicular edge momentum by drift-interchange turbulence and blobs. Physics of Plasmas, 15(3):032304, 2008.

[37] J. S. E. Portela, I. L. Caldas, R. L. Viana, and P. J. Morrison. Diffusive Transport Through a Nontwist Barrier in Tokamaks. International Journal of Bifurcation and Chaos, 17(05):1589–1598, May 2007.

[38] J. S.E. Portela, I. L. Caldas, and R. L. Viana. Tokamak magnetic field lines described by simple maps. The European Physical Journal Special Topics, 165(1):195–210, December 2008.

[39] Jefferson S E Portela, E Iber, Instituto De F, Ricardo L Viana, Universidad Rey, and Juan Carlos. FRACTAL AND WADA EXIT BASIN BOUNDARIES IN TOKAMAKS. 17(11):4067–4079, 2007.

[40] D. Reiser. Impact of large island perturbations on turbulent blob transport in tokamaks. Physics of Plasmas, 14(8):082314, 2007.

[41] Marshall N Rosenbluth and Albert Simon. Finite larmor radius equations with nonuniform electric fields and velocities. Physics of Fluids, 8:1300, 1965.

[42] M.N. Rosenbluth, R.Z. Sagdeev, J.B. Taylor, and G.M. Zaslavski. Destruction of magnetic surfaces by magnetic field irregularities. Nuclear Fusion, 6(4):297, 1966.

[43] D. A. Russell, J. R. Myra, and D. A. D'Ippolito. Saturation mechanisms for edge turbulence. Physics of Plasmas, 16(12):122304, 2009.

[44] Y Sarazin and Ph. Ghendrih. Intermittent particle transport in two-dimensional edge turbulence. Physics of Plasmas, 5(12):4214–4228, 1998.

[45] M.V. Umansky, X.Q. Xu, B. Dudson, L.L. LoDestro, and J.R. Myra. Status and verification of edge plasma turbulence code BOUT. Computer Physics Communications, 180(6):887–903, June 2009.

[46] J.G. Watkins, T.E. Evans, C.J. Lasnier, R.a. Moyer, and D.L. Rudakov. Target plate conditions during stochastic boundary operation on DIII-D. Journal of Nuclear Materials, 363-365:708–712, June 2007.

[47] G.S. Xu, V. Naulin, W. Fundamenski, C. Hidalgo, J.A. Alonso, C. Silva, B. Gonçalves, A.H. Nielsen, J. Juul Rasmussen, S.I. Krasheninnikov, B.N. Wan, M. Stamp, and JET EFDA Contributors. Blob/hole formation and zonal-flow generation in the edge plasma of the jet tokamak. Nuclear Fusion, 49(9):092002, 2009.

[48] M. Yagi and W. Horton. Reduced Braginskii equations. Physics of Plasmas, 1(7):2135, 1994.

[49] N. Yan, A. H. Nielsen, G. S. Xu, V. Naulin, J. Rasmussen, and J. Madsen. Measurement and simulation of intermittent characteristicsin the boundary plasma of east tokamak. 40th EPS Conference on Plasma Physics, 37D:8028–8056, july 2013.

[50] G. Q. Yu and S. I. Krasheninnikov. Dynamics of blobs in scrape-off-layer/shadow regions of tokamaks and linear devices. Physics of Plasmas, 10(11):4413, 2003.

[51] G. Q. Yu, S. I. Krasheninnikov, and P. N. Guzdar. Two-dimensional modelling of blob dynamics in tokamak edge plasmas. Physics of Plasmas, 13(4):042508, 2006.